https://doi.org/10.5194/egusphere-2025-6379
Preprint. Discussion started: 21 January 2026

Arctic sea ice predictability on daily-to-weekly timescales: sensitivity to initial positional errors under different rheology formulations

Lohenn Fiol[1], Stephanie Leroux[1], Pierre Rampal[2], and Jean-Michel Brankart[2]
[1]DATLAS, Grenoble, France
[2]Institut des Géosciences de l'Environnement, CNRS, Grenoble, France
Correspondence: Lohenn Fiol (fioll@univ-grenoble-alpes.fr)

Abstract. We investigates short-term (daily-to-weekly) winter Arctic sea-ice predictability using a coupled ice–ocean model, and focusing on how sensitive forecasts are to initial uncertainty in the location of sea ice features (e.g., leads, ridges, etc.). In this context, two rheologies are compared: elastic–viscous–plastic (aEVP) and brittle Bingham–Maxwell (BBM). For January–March 1997, we conduct 10-day ensemble forecasts, initialized by applying displacement perturbations to all sea-ice fields to represent initial positional errors, while keeping atmospheric forcing identical for all the ensemble members. Potential predictability is evaluated using a "perfect model" framework and probabilistic metrics for the ice-edge position errors, local state-variable errors (concentration, thickness, drift, deformation), and the spread of virtual drifters. Ice-edge forecasts are found to be largely insensitive to initial positional errors for both rheologies, indicating dominance of thermodynamic forcing rather than ice dynamics at short lead times. In contrast, BBM exhibits strong nonlinear sensitivity in pack ice: predictability is limited to 1–5 days for drift and deformation and 5–10 days for concentration. The aEVP model, on the other hand, quickly damps small-scale heterogeneities, yielding more convergent, and thus more predictable solutions. These findings have concrete implications: the BBM model produces larger regions with high probability of intense deformation and the spread of Lagrangian drifters up to an order of magnitude greater than in the aEVP model. Our results underscore the importance of ensemble forecasting for quantifying risks in a highly nonlinear and weakly predictable sea-ice system.

1 Introduction

The demand for reliable daily-to-weekly operational forecasts of sea ice conditions in polar regions is growing. Such forecasts are crucial for mitigating risks and ensuring safe navigation and effective response in case of a pollution event, particularly in light of the marked rise in human activity in these areas over the last decade. The Arctic Shipping Status Report #1 (PAME, 2024) reports a 37% increase in the number of ships entering the Arctic Ocean between 2013 and 2023, while the total cumulative distance sailed by vessels in the Arctic has doubled. At the same time, Tietsche et al. (2020) emphasized that substantial gaps persist between existing operational sea ice forecast products and the level of quality and relevance required by end-users.

In practice, an operational sea ice forecasting system is affected by numerous sources of uncertainty that limit its ability to accurately predict the future evolution of the physical sea ice state. For a given metric, lead time, and system configuration, the upper bound of attainable forecast skill is often termed the *practical predictability* of that system (e.g. Korosov et al., 2023). Uncertainty stems from three main sources: (i) the sea ice model itself, including its numerical approximations and parameterizations; (ii) uncertainty in the external drivers of the system, specifically the atmospheric and oceanic conditions in the case of sea ice; and (iii) uncertainty in the initial sea ice state used to start the forecast. This last source of uncertainty, often termed *initial uncertainty*, arises both from the numerical approximations involved in the Data Assimilation (DA) process and from the incomplete coverage and limited accuracy of available observations in space and time. Furthermore, due to the strongly non-linear character of the equations governing the physical system, even minimizing initial errors as much as possible does not yield a perfectly accurate forecast. Put differently, any arbitrarily small initial error will ultimately be amplified and will degrade the forecast accuracy (e.g. Bertino et al., 2025; Reifenberg and Goessling, 2022). As a result, one can introduce a *finite predictability horizon* (also called *intrinsic* or *potential predictability*), as is commonly done in weather prediction and other chaotic systems (e.g. Lorenz, 1969, 1975). Potential predictability represents the theoretical upper limit of forecast skill that could be attained if all other sources of error in the numerical model and its external forcings were eliminated.

Assessing the potential predictability of relevant sea ice metrics can inform the prioritization of future model improvements and offer an estimate of the forecast-skill gains that might be achieved for a specific application. Predictability studies can likewise improve our knowledge of the physical system itself and of the constraints introduced by its numerical representation. In particular, existing ocean–sea-ice operational forecasting systems differ in how they numerically formulate sea-ice rheology, that is, in how they describe the relationship between stress and strain in the ice. Bertino et al. (2025) distinguishes two main groups: (i) the elastic–viscous–plastic (EVP) framework originating from Hibler (1979) and subsequently extended, for instance, by Hunke and Dukowicz (1997); Kimmritz et al. (2016), and (ii) the more recently introduced brittle Bingham–Maxwell (BBM) framework (Ólason et al., 2022), which builds on earlier work by Girard et al. (2011); Dansereau et al. (2017) and the references therein. The BBM rheology was developed to more realistically capture the linear deformation patterns in sea ice that are linked to the formation of ridges and leads (also referred to as Linear Kinetic Features), as well as the observed spatial and temporal scaling characteristics of sea-ice deformation (Rampal et al., 2008, 2019, and references therein). To our knowledge, however, the consequences of these different rheological frameworks for the predictability of sea-ice dynamics have not yet been examined and will be investigated in this study.

Several facets of sea-ice predictability on daily to weekly timescales have already been explored in previous work. Mohammadi-Aragh et al. (2018) derived initial estimates of a practical predictability horizon of 4–8 days for linear kinematic features, based on EVP-based MITgcm ensemble simulations, whereas Korosov et al. (2023) identified a practical predictability limit of roughly 3–4 days for sea-ice deformation in the BBM-based neXtSIM model. Overall, it has been demonstrated that the primary contributor to sea-ice forecast uncertainty is the uncertainty in surface wind forcing (Mohammadi-Aragh et al., 2018; Rabatel et al., 2018; Cheng et al., 2020). In these studies, wind uncertainty was represented either as Gaussian perturbations to the wind field, correlated in space and time, or through the use of individual members of the ECMWF Ensemble Prediction System. More specifically, Mohammadi-Aragh et al. (2018) showed that atmospheric uncertainty overwhelms initial sea-ice errors, which in their framework were introduced solely by spatially correlated perturbations of the initial sea-ice thickness.

Cheng et al. (2020) also found that wind uncertainty dominates over model uncertainty, the latter being incorporated by applying random spatial perturbations to the initial ice cohesion field.

At the same time, uncertainty in the initial conditions, although less influential than uncertainty in the surface winds, should not be overlooked. Rabatel et al. (2018) and Cheng et al. (2020) pointed out that, at local spatial scales and for short prediction lead times, variability in the Lagrangian motion of sea-ice drifters is likely driven not only by atmospheric forcing, but also by inaccuracies in the initial location and orientation of the existing sea-ice fracture network. In the present study, we specifically investigate how sensitive the sea-ice system is to uncertainty in the initial positions of sea-ice features such as leads, ridges, and shear lines. The purpose is to compare how the two types of rheological formulations, EVP and BBM, respond to initial positional uncertainties and to examine the implications of these differences for short-term sea ice forecasting.

Some recent work, such as Korosov et al. (2023) or Moro et al. (2024), has focused on practical predictability within given operational systems and explored how improvements in data assimilation to reduce initial-condition errors can impact forecast skill. In contrast, we adopt a complementary approach, examining the potential predictability of the sea-ice system: within a "perfect-model" framework (e.g., Reifenberg and Goessling, 2022), we introduce positional perturbations at initialization into a sea-ice model and atmospheric forcing both assumed perfect. Using an ensemble approach, we then track how these initial positional errors develop over time and influence the forecast skill across multiple sea-ice-relevant metrics. By systematically varying the magnitude of the initial positional uncertainty from large to small, we assess the highest achievable forecast accuracy as a function of both lead time and initial error. This is our definition for predictability, or to put it differently, the maximum possible skill for a given metric and lead time, under the assumption that all sources of uncertainty other than the imposed initial positional error have been eliminated.

By construction, our framework separates out the inherent nonlinear behavior of the sea-ice system itself. Specifically, we assume that the atmospheric forcing is perfectly known, which does not reflect operational forecasting settings where several uncertainty sources interact. Our purpose is therefore not to mimic realistic operational errors, but to evaluate the maximum level of predictability constrained solely by sea-ice dynamics, prior to accounting for its coupling with the chaotic atmosphere.

Note also that this paper focuses on a daily-to-weekly forecasting horizon, and our methodology contrasts with earlier work that explored sea ice predictability on longer timescales (subseasonal to interannual) using fully-coupled climate models (ocean–sea ice–atmosphere). Those previous studies evaluated predictive skill over several weeks to months and for spatially integrated climate-relevant quantities, such as sea ice area, extent, and volume (e.g. Day et al., 2014; Cruz-García et al., 2019), the sea ice edge (e.g. Tietsche et al., 2014; Goessling et al., 2016; Goessling and Jung, 2018; Zampieri et al., 2018), and seasonal drift Reifenberg and Goessling (2022). However, none of them explicitly investigates how the choice of rheology formulation affects predictability, and their coupled atmosphere–ice–ocean modeling setups do not allow one to separate the uncertainty associated with the chaotic atmosphere from that stemming from the inherently non-linear response of the sea ice itself.

Section 2 provides a description of the model and experimental design used in the present study. An evaluation of the modeled sea ice drift is provided in Sect. 3, and the predictability results are presented and discussed in Sect. 4. Finally, concluding remarks are proposed in Sect. 5.

https://doi.org/10.5194/egusphere-2025-6379
Preprint. Discussion started: 21 January 2026

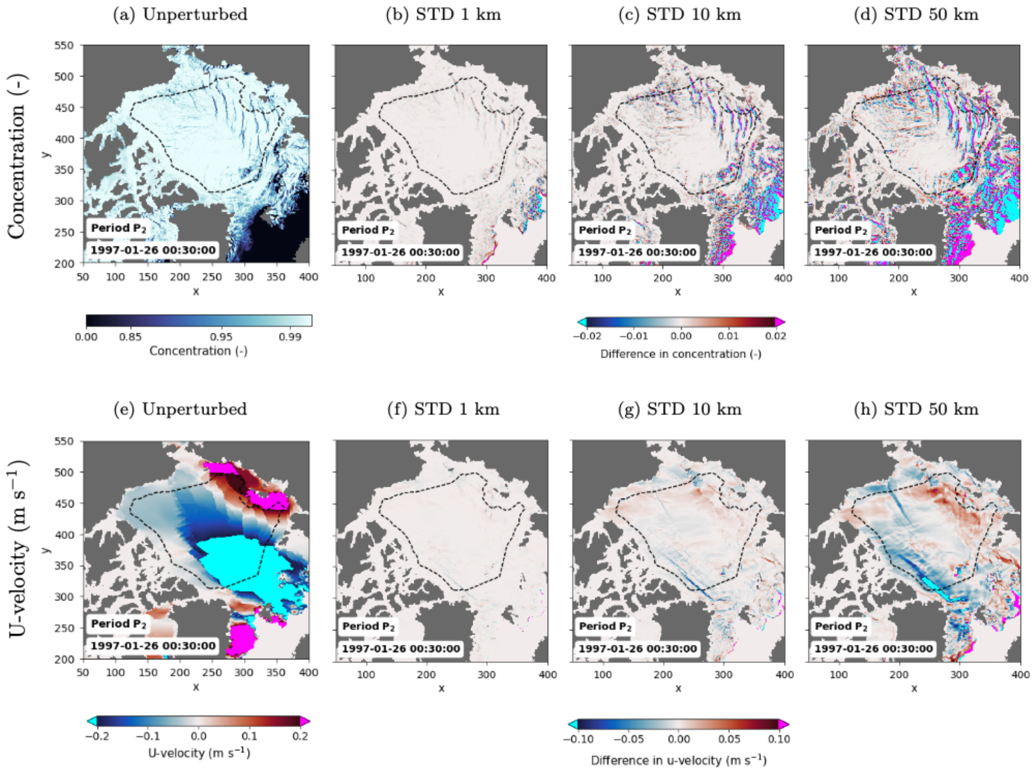

Figure 1. Unperturbed initial states in (a) sea ice concentration and (e) the U-component of sea ice velocity at the beginning of period P_2 (t_0: 1997-01-26) from the unperturbed reference experiment with the BBM model. Panels (b-d) and (f-h) show the difference in the initial states of two perturbed ensemble members for concentration and the U-component of sea ice velocity, respectively. Panels (b,f), (c,g), and (d,h) correspond to initial perturbations scaled for a standard deviation (STD) of 1 km, 10 km and 50 km, respectively. The black dashed line defines the boundaries of the region over which the ensemble scores for the pack ice (Sect. 4.2) are computed.

https://doi.org/10.5194/egusphere-2025-6379
Preprint. Discussion started: 21 January 2026

Model configuration			
Ocean–sea ice model:	NEMO + SI^3 v4.2.2		
Domain:	Full Arctic region (down to about 40° N in the Atlantic)		
Horizontal resolution:	1/4°		
Horizontal size in grid points (x x y):	492 x 566		
Number of vertical levels:	31		
Sea ice rheology formulation:	aEVP (Kimmritz et al., 2016)		BBM (Brodeau et al., 2024)
Air-ice drag coefficient:	1.1×10^{-3}		2.1×10^{-3}
Atmospheric forcing			
Forcing dataset:	Hourly ERA5 reanalyses (Hersbach et al., 2020)		
Ensemble configuration			
Number of members:	20		
Perturbation type:	Initial positional perturbations applied to the sea ice state from reference simulation		
Perturbation amplitude scaled to:	STD 1 km	STD 10 km	STD 50 km
Hindcast periods			
Period length:	10 days each		
Period start dates	P_1:1997-01-16 – P_2:1997-01-26 – P_3:1997-02-05 – P_4:1997-02-15		
(1997-MM-DD) :	P_5: 1997-02-25 – P_6:1997-03-07 – P_7:1997-03-17 – P_8:1997-03-27		

Table 1. Summary of the experimental set-up. See text in Sect. 2 for more details.

2 Experimental setup

2.1 The coupled sea ice–ocean model

We use the SI^3 sea ice model (Sea Ice modelling Integrated Initiative, Vancoppenolle et al., 2023) coupled with the Boussinesq hydrostatic ocean model NEMO (Nucleus for European Modelling of the Ocean, Madec and the NEMO-System-Team, 2024). SI^3 is an Eulerian continuous thermodynamical model of sea ice that we use here with five different thickness categories. In this model, the drift and deformation of sea ice are solely horizontal and the heat transfer is only vertical due to the scale ratio between the width ($\mathcal{O}$(100-1000 km)) and the thickness of the sea ice ($\mathcal{O}$(1 m)).

We use a regional configuration of SI^3 -NEMO covering the Arctic region, from the Bering Strait down to about 40° N in the Atlantic Ocean (the model domain is partially shown in Fig. 1, with truncation indicated by the grid-point ticks on the x and y-axes). The configuration is based on a horizontal resolution of $1/4°$ (i.e. about 10 km in the central Arctic region) and 31 vertical levels for the ocean. This regional configuration is the same as in Brodeau et al. (2024), who have implemented and evaluated an elasto-brittle formulation for sea ice rheology (i.e. the BBM formulation, as described in Ólason et al. (2022)) in addition to the already existing elasto-visco-plastic formulation (aEVP, Kimmritz et al., 2016).

We take advantage of this single modelling framework in which either the BBM or the aEVP rheology formulation can be set to test the impact of rheology on the short-term predictability properties of the system. Hindcast experiments are thus run both with the BBM and aEVP rheology, while all other settings are kept the same in the modelling framework, namely same atmospheric forcing, same resolution, same ocean model parameters, and allows a clean comparison framework.

The main parameters and settings used in this study are summarized in Table 1. The only exception is the air–ice drag coefficient (parameter `rn_Cd_i` in the SI^3-NEMO namelist), which we have adjusted separately in the experiments with BBM and aEVP, as also done by Brodeau et al. (2024), to establish a fair comparison framework and ensure that both configurations had a realistic mean drift over the period of interest. The air–ice drag parameter plays an important role in computing the surface momentum fluxes based on the sea ice state and the prescribed surface atmospheric forcing. Previous studies showed that the simulated drift of sea ice is sensitive to the way air-ice drag is set (e.g. Rampal et al., 2016; Rabatel et al., 2018; Cheng et al., 2020), and recommended fitting its value according to an observed metric typically based on sea ice drift or deformation. In this study, we used a drag coefficient of 2.10×10^{-3} in the BBM-based experiments and 1.10×10^{-3} with aEVP. These values were tuned so that the mean simulated sea ice drift in the BBM and aEVP configurations—averaged over January–February–March 1997 and over the pack-ice region (Fig. 1)—matches the corresponding observed mean (i.e., 5.2 km / 24 h) within ±0.2 km / 24 h, which was estimated from the EUMETSAT OSI-SAF daily gridded sea ice drift product (OSI-455, Lavergne and Down, 2023).

2.2 The set of ensemble hindcasts

Building on the work of Brodeau et al. (2024), we focus on the same 1997 winter season in January-March as their study, where they implemented the BBM rheology formulation in the SI^3 model and thoroughly compared the resulting sea ice scaling properties of deformation with those of the standard aEVP formulation and with the RGPS (RADARSAT Geophysical Processor System Lagrangian trajectories) observation dataset available for that year (Kwok et al., 1998; Kwok, 2001). We provide below some additional evaluation of the regional model on local sea ice drift as seen from a Lagrangian-drifter point of view (Sect. 3).

Our predictability study aims to contrast the behaviour of BBM and aEVP models, and thus focuses on the winter months (Janurary to March), when friction and internal forces in the sea ice—in other words, rheology—play a crucial role in how the ice behaves, compared to later in the season when the so-called "free drift" regime may take over when the ice responds more directly to the wind forcing as a consequence of low internal stresses within the ice (Rabatel et al., 2018).

Predictability is assessed by running a set of 10-day ensemble hindcasts with N=20 members initialized with perturbed sea ice states. The number of members in the ensemble is a compromise between computational cost and the robustness of the obtained ensemble statistics. We built on Cheng et al. (2020) who showed, in a similar context (but with a different model), that their ensemble hindcast statistics converged when the ensemble size exceeded 20.

The ensemble hindcasts are initialized at different start dates sampled within the 1997 January-March season so that eight consecutive, non-overlapping 10-day ensemble hindcasts are run in total over the period. These periods are labeled P1, P2,..., P8 hereafter, and their start dates are summarized in Table 1. The sea-ice-ocean initial state of each of these periods is extracted from a single, unperturbed simulation of 3 months (hereafter the "unperturbed reference simulation") based on the BBM rheology formulation. It is important to note that all the ensemble hindcasts run in this study, using either the BBM or the aEVP rheology formulation, are initialized from exactly the same set of initial states taken from the BBM-based reference simulation and subsequently perturbed. This choice ensures that the extracted initial states include a realistic level of heterogenities and LKFs as it would be in an operational context where data assimilation would assimilate high-resolution observations as envisaged by, e.g. Korosov et al. (2023) or Moro et al. (2024).

The reference simulation begins on January 1, initialized with the GLORYS12 reanalysis product (Lellouche et al., 2021) for both ocean and sea ice states. The first ensemble hindcast run over P1 (start date on January 16) is thus started after a spinup of 15 days. Given the rapidity with which the dynamics of sea ice evolve in the BBM-based configuration, this short spinup was enough for most sea ice variables, as will be shown by the results of this study. Only for sea ice thickness, we have observed in our results some indications that the modeled thickness had not reached its equilibrium regime, even though it does not limit our ability to draw some conclusions regarding predictability (as discussed in Sect. 4.2).

Ensemble scores are finally computed from the ensemble hindcasts to assess the predictability horizon in the BBM-based and aEVP-based configurations. The ensemble scores are all computed from hourly-averaged model outputs unless stated otherwise. For this reason, in our results, the time indication t_0 corresponds to the state of the model averaged over the first hour of simulation (which is not strictly equivalent to the initial state, but close enough to make the approximation, except where explicitly noted in the text).

2.3 Initial positional uncertainty

The initial states sampled from the unperturbed simulation are perturbed to initialize the ensembles with positional errors and mimic possible misfits in the position of the sea ice features at initial time in an operational context. We do so by generating maps of random displacements $\Delta\mathrm{x}(x,y)$, $\Delta\mathrm{y}(x,y)$ that are then applied to perturb consistently the initial condition of all the sea ice variables (i.e. using the same maps of displacements for all the variables).

Compared to more standard perturbation methods, which usually apply Gaussian perturbations to the model variables in a specific modal subspace, (Empirical Orthogonal Functions, singular vectors, bred vectors, etc.), the proposed method has the originality to produce non-Gaussian perturbations of the geophysical fields through Gaussian displacement perturbations. It is particularly relevant in the context of this study, where we aim to investigate specifically the sensitivity of the system to small displacements in the location of sea ice structures (LKFs, leads, etc) rather than to large amplitude variations in the sea ice fields.

In practice, we use the Lu-generator python package (Brankart and Leroux, 2025) to generate and apply these perturbations to the SI^3 initial sea ice states (in this study, only the sea ice state is perturbed, the ocean state is left unperturbed). We generate a set of N=20 maps for $\Delta\mathrm{x}(x,y)$ and $\Delta\mathrm{y}(x,y)$, consisting of normal isotropic random vectors with a spatial correlation scale of 500 km (about 1/5th of the size of the Arctic basin) and a standard deviation of 1 km, 10 km, or 50 km, corresponding to the 3 amplitudes of displacement (small/medium/large) that will be used in the experiments. In practice, for better comparison, we use the same sample of 20 displacement maps to initialize all the ensemble experiments (all start dates and all three amplitudes),

https://doi.org/10.5194/egusphere-2025-6379
Preprint. Discussion started: 21 January 2026

with a simple rescaling of the standard deviation for each amplitude. The "small", 1-km perturbation is scaled to about 1/10th of the size of a grid cell in our system, to represent a lower bound error, where initial sea ice features are only very slightly displaced relative to the system resolution. On the other hand, the "medium" and "large" perturbations (10-km and 50-km resp.) represent shifts of about 1 (resp. 5) grid cells in average. We will comment further on the amplitude of these initial perturbations when analyzing the different ensemble scores and relate them to existing errors in the current operation systems for comparison, when this information is available in the literature.

An example of the resulting perturbed initial states is shown in Fig. 1 for the concentration and the U-component of the drift, plotting the unperturbed fields (left column) and the difference between two perturbed members (right columns). Leads, LKFs, and patterns of positive/negative drift in the initial fields are slightly shifted and distorted between the two ensemble members, in order to take into account some uncertainty in their exact location at initial time. This positional uncertainty is by design scaled to the imposed displacements. Note that the perturbations are applied everywhere in the domain, except over land and at and near the coast, where they are damped to zero to avoid displacing the sea ice unrealistically at the coast and over land. The damping coefficient is set to zero at the coast and grows exponentially offshore to 1 with a characteristic distance of about 25 grid points (about 250 km).

3 Evaluation of the modeled sea ice drift

Before assessing the predictability of the system in its two configurations (BBM and aEVP), we first provide a brief evaluation against available observations. The assessment of sea-ice deformation has already been carried out in Brodeau et al. (2024), who analyzed the scaling properties of deformation in configurations very close to those used here and compared them with the RGPS Lagrangian-trajectory dataset (Kwok et al., 1998; Kwok, 2001). In this section, we therefore limit ourselves to checking the realism of the simulated sea-ice drift at local scales, using Lagrangian trajectories from the International Arctic Buoy Programme (IABP) (2023) dataset. Although the mean sea-ice drift in both configurations—averaged over the 3-month period and over the pack-ice region—was tuned to match the observed OSI-SAF mean (through adjustment of the air–ice drag coefficient; see Sect. 2), this tuning does not guaranty a perfect consistency with local drift observations from an independent data set such as the IABP data set. Overall, the goal of this brief evaluation is to verify that both configurations produce a sufficiently-realistic and well-tuned representation of the sea-ice drift at local scales to then allow a fair comparison of their predictability properties in the following sections.

We used ice buoys from the IABP data set within the study period (Jan-Mar 1997). These buoys are fixed on sea ice and record their drifting position over time. In 1997, positions are given every 3 hours with an uncertainty of 100-300 m (Rampal, 2008). We have selected the buoys available over the eight 10-day consecutive periods P1,..., P8, rejecting those that have more than 10% missing values over a given period. We have also rejected all the buoys for which the position at the initial time of the given period is missing. Furthermore, we have filtered out a few buoys with obvious non-physical trajectories. In the end, 101 buoys were selected for Jan-Mar 1997 following our criteria, all localised in the central Arctic region, even though not evenly distributed, with more buoys in the vicinity of the North Pole (Fig. 2).

https://doi.org/10.5194/egusphere-2025-6379
Preprint. Discussion started: 21 January 2026

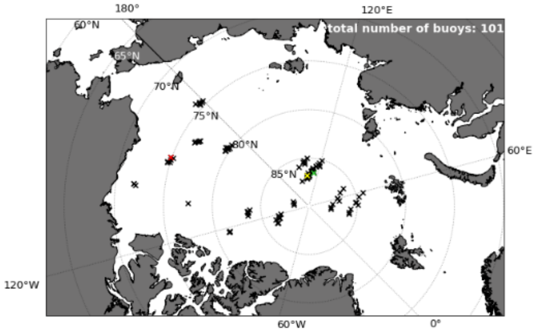

Figure 2. Location of the observed IABP buoys at initial time of the P1,...,P8 hindcast periods (start dates from the 16th of January to the 27th of March 1997, see Table 1). 101 IABP buoys are considered in total. The colored "x" markers highlight the initial position of the few buoys taken as examples in the following (Figs. 4 and 13).

To compare the Eulerian model drift with the IABP Lagrangian observations, we generate virtual buoy trajectories: at initial time of each P1,...,P8 period, virtual buoys are seeded at the positions of the real IABP buoys available and selected for this given period (see their initial location in Fig. 2). The virtual buoys are then advected for 10 days based on the hourly-averaged sea ice velocity fields using the Sitrack package (Brodeau, 2025). Thus, 10-day trajectories are produced, sampling the position of these virtual buoys every hour. The virtual trajectories have been generated for the 8 periods and the N=20 members of the ensemble hindcasts initialized with the 3 types of perturbation amplitudes, but only the results based on the 10-km perturbations are shown below for the sake of brevity, as the conclusions were similar for all.

Figure 3 shows some statistical evaluation metrics that compare the virtual buoys seeded in the model with the observed ones. The distance covered by the simulated buoys (Fig. 3a) is on the order of 60 km on average after 10 days, consistent with the observed distance, although on average the simulated buoys cover a slightly longer distance than their corresponding observed buoy (about 5 km longer after 10 days for both model configurations). Figure 3b also shows the difference in the direction of propagation, as measured by the angle between the two lines drawn from the seeding position to the observed buoy and the barycenter of the N=20 simulated buoys of each ensemble hindcast. We find an absolute error of about 20° in the direction of propagation of the barycenters, on average, compared to the direction of the observed buoys. Interestingly, the angle error cancels out in average for the BBM-based simulated trajectories if we consider the relative angles, while a 10° clockwise bias remains in the aEVP trajectories relative to the observations. Note that if on average the properties of the virtual buoys remain close to the observed, there is some diversity in individual cases both in the direction of propagation and in the distance covered, as illustrated by the examples in Fig. 4. The error in the position of the simulated buoys, measured as the distance between the observed buoy and the barycenter of the virtual buoys, is shown in Fig. 3c. The distance grows with lead time, as expected from any unperfect forecast, and on average after 10 days, it represents a mean error of about 15 km in the position of the barycenter compared to the observed. Note that this amount of error is consistent with the error found by

https://doi.org/10.5194/egusphere-2025-6379
Preprint. Discussion started: 21 January 2026

(a) Length of the trajectories

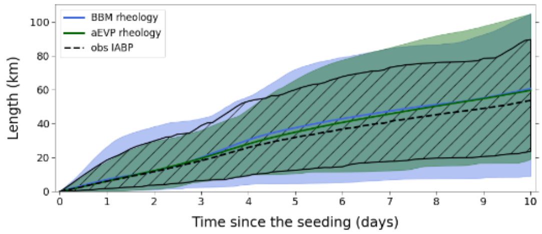

(b) Angle between observations and barycenters

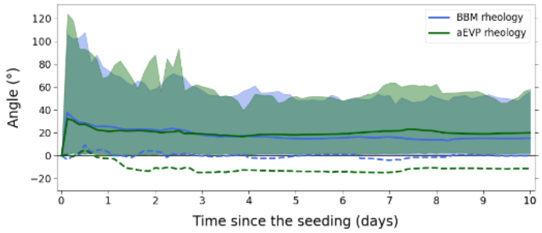

(c) Distance between observations and barycenters

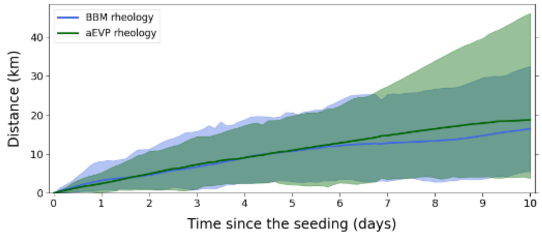

Figure 3. Temporal evolution of different properties of the simulated buoys compared to the observed IABP buoys: (a) length, i.e., the distance covered by the buoys, (b) angle between the two lines drawn from the seeding position to, respectively, the observed buoy and the barycentre of the N = 20 simulated buoys of each ensemble hindcast, and (c) the direct distance between the observed buoy and the barycentre. The results of BBM and aEVP are colored blue and green, respectively, with the thick lines for the ensemble means of all the buoys over all eight 10-day periods, while the shaded envelopes indicate the 5%-to-95% percentile ensemble distribution. In (a) the distance covered by the observed buoys is with the black line (mean) and the hatched envelope (5%-to-95% percentile). In (b), the envelopes and solid lines are computed considering the absolute value of the angle, while the dashed lines correspond to the mean value of the angle.

Rabatel et al. (2018); Cheng et al. (2020) from the virtual trajectories produced by their model BBM-based NeXtSIM. This 230 error appears to be slightly larger in the aEVP model (about 19 km after 10 days). Note also that from the example trajectories

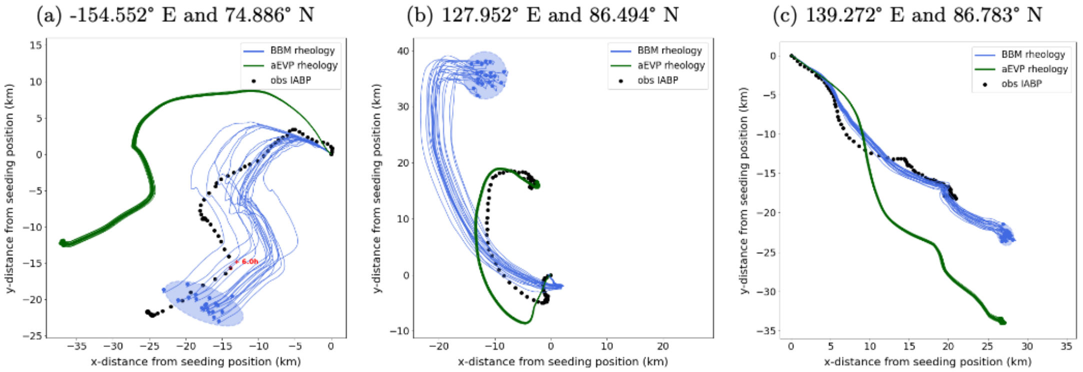

Figure 4. Three examples of observed IABP trajectories (black) and corresponding virtual trajectories simulated from the BBM ensemble hindcast (blue, 20 members) and aEVP ensemble hindcast (green, 20 members) seeded at midnight on: (a) March 7th, at -154.552° E;74.886° N (red cross in Fig. 2), (b) February 15th, at 127.952° E;86.494° N (green cross in Fig. 2), and (c) February 5th, at 139.272° E; 86.783° N (yellow cross in Fig. 2). The observed IABP trajectories are plotted with a plain black circle every 3 hours. In case of missing values, the circle following the gap is shown in red, with the corresponding time gap. The simulated ensemble trajectories are plotted as colored curves, and only the final positions after 10 days are marked as plain circles. The shaded ellipses represent the 95% confidence regions of the final positions, assuming a bivariate normal distribution.

in Fig. 4, it appears that the spread in the virtual buoy ensemble generated from the aEVP model is smaller than the spread in the BBM ensemble. This aspect will be further documented and discussed in Sect. 4.3.

Overall, this evaluation confirms that both configurations simulate the observed drift with sufficient realism to be used in the predictability analysis that follows. Some additional Lagrangian metrics will be presented and discussed in Sect. 4.3 to illustrate the difference in the predictability properties of the two configurations.

4 Daily-to-weekly predictability of the sea ice system

We now investigate the daily-to-weekly predictability properties of the sea ice system with either type of rheology, focusing on its sensitivity to initial uncertainty in the position of sea ice features. We consider here three different types of metrics or scores to measure the dispersion of the ensemble hindcasts, and to quantify the system skill regarding those three metrics (considering a "perfect model" framework with no other sources of uncertainty than initial uncertainty, as explained in Sect. 2).

4.1 Predictability of the sea ice edge

We first focus on the predictability of the position of the sea ice edge. The sea-ice edge marks the boundary between the ocean covered with ice and the open ocean. As such, it is a widely used proxy for sea-ice extent and its variability in climate and seasonal prediction studies (e.g., Tietsche et al., 2014; Goessling et al., 2016; Goessling and Jung, 2018; Zampieri et al., 2018), and at shorter lead times it is a routinely-evaluated forecast product from operational sea-ice prediction systems (e.g., Williams et al., 2021). In this study, based on the ensemble hindcast experiments, we can compute a probabilistic version of the Integrated Ice-Edge Error (IIEE, Goessling et al., 2016), namely the Spatial Probability Score applied to the sea ice edge (thereafter SPS, Goessling and Jung, 2018). It is defined as:

$$\mathrm{SPS} = \int\limits_{x}\int\limits_{y}\Big[P[c > 0.15](x,y) - P[c > 0.15]_{\mathrm{ref}}(x,y)\Big]^2 dxdy \tag{1}$$

where it represents the spatial integral of the square difference between $P[c > 0.15](x,y)$ the probability of having a concentration greater than 0.15 at a given location (x,y) in the ensemble forecast, and $P[c > 0.15]_{\mathrm{ref}}(x,y)$ the same probability but for a given reference. We use the usual 0.15 concentration threshold to define the location of the ice edge, as in, e.g., Goessling et al. (2016); Goessling and Jung (2018); Zampieri et al. (2018); Williams et al. (2021). The probabilities $P[c > 0.15]$ and $P[c > 0.15]_{\mathrm{ref}}$ are estimated from the discretized frequency of the event. Since we follow a perfect model approach, the reference is taken alternatively as a member of the ensemble and $P[c > 0.15]_{\mathrm{ref}}$ takes the value of 0 or 1. $P[c > 0.15]$ is computed considering the 19 remaining members of the ensemble and can take a continuum of values between 0 and 1. Examples of the corresponding probability maps are depicted in a subregion near Svalbard in Fig. 5 and will be commented on in more detail in the following.

Our method of perturbing the initial state acts consistently on all sea ice fields and not specifically on the ice edge. An example is given in Fig. 6 to illustrate how the initial perturbations of concentration, drift, thickness, etc., translate into an ensemble spread in the position of the local sea ice edge in a subregion near Svalbard. Overall, the initial spread in the position of the sea ice edge is consistent with the scaling of the positional displacements applied to the sea ice state: when the perturbation is scaled to 1 km (about 1/10th of the size of the model cell), the sea ice edge shows almost no spread in its local position (Fig. 6a). For a perturbation scaled to 10 km, the edge of the sea ice is spread locally by a few grid cells between the ensemble members (Fig. 6b). In the 50 km case (Fig. 6c), the position of the sea ice edge can differ by up to 15-20 grid cells locally (up to 200 km).

Integrated across the entire domain, the initial spread between members, quantified by the SPS score in Fig. 7, ranges from 0.15 to 47 $\times 10^4$ km^2 depending on the initial date and ensemble members. It should be noted that the largest initial errors we generate in the SPS in this study are of the same order of magnitude as the practical initial errors in the coupled climate systems (atmosphere–ice-ocean) of the subseasonal-to-seasonal (S2S) database investigated by Zampieri et al. (2018), where the initial error ranges between 20 and 70 $\times 10^4$ km^2 and their climatological reference is about 55 $\times 10^4$ km^2. In their climate-coupled setups, the initial error in the sea ice edge is highly influenced by the initialisation strategies of the 3-D ocean (which differ from one coupled system to another) and can lead to relatively large errors, close to (or sometimes even larger than) the climatological reference. Regional operational sea ice forecasting systems, such as NeXtSIM-F (Williams et al., 2021) can do better to initialize the sea ice edge in a single sea ice configuration forced by the operational regional ocean product TOPAZv4 (Sakov et al., 2012; Simonsen et al., 2018). For reference, the initial error in the IIEE (which is the deterministic version of the SPS) is given to about 7-10 $\times 10^4$ km^2 for the January-March period of year 2019 in Williams et al. (2021), which falls again in

https://doi.org/10.5194/egusphere-2025-6379
Preprint. Discussion started: 21 January 2026

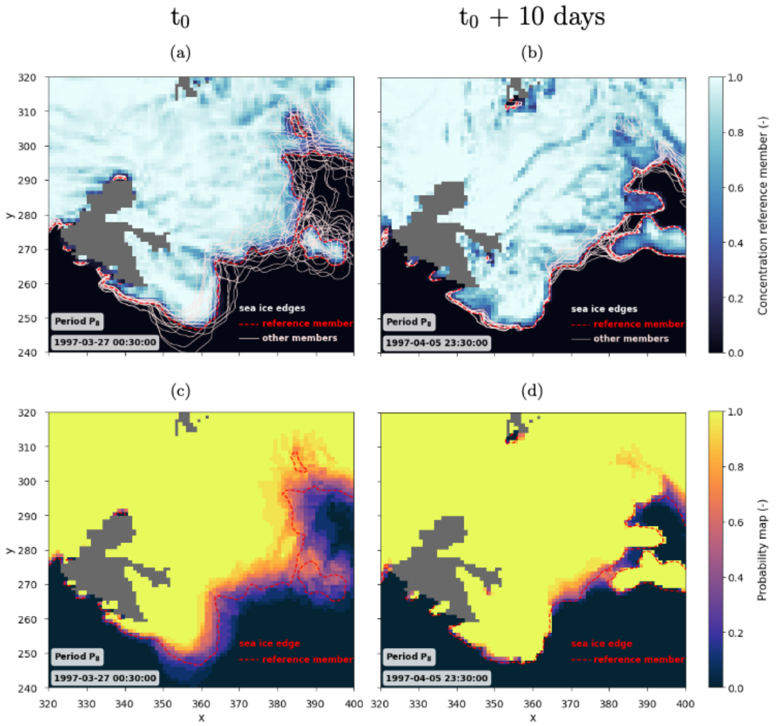

Figure 5. Example of the dispersion of the sea ice edge position (pink and red lines) in the Svalbard region in the BBM ensemble members for period P_8 and from the 50-km-scaled perturbation, at initial time t_0 and after 10 days (a,b respectively). The hourly sea ice concentration field of the reference member is shown in the background for their respective lead time (shading in a, b). The corresponding maps of probability $P[c > 0.15]$, computed from the 19 members excluding the chosen reference member (whose ice edge is shown in red) are also plotted at initial time and after 10 days (c,d resp.) to illustrate the methodology to compute the SPS metrics (see text for more details).

the range of the initial errors we have generated on the sea ice edge. Overall, we thus verify here that the approach we propose in this paper generates initial errors in the SPS whose amplitudes range from those typically observed in current climate and operational sea ice forecasting systems to very small local errors in the ice-edge position (kilometer scale, i.e., smaller than a model grid cell). This makes us able to study the sensitivity of the sea ice system to initial errors.

The evolution of the SPS error in the ensemble forecasts is plotted as a function of lead time, for the BBM and aEVP experiments separately (Fig. 7). Each plotted curve corresponds to the SPS score for one of the eight forecast periods, computed by taking one member of the 20 ensemble members as the pseudo-truth (resulting in a total of 8 periods × 20 scores = 160 curves in each panel of Fig. 7). In all experiments, we find that the SPS error systematically decreases with time (or remains

https://doi.org/10.5194/egusphere-2025-6379
Preprint. Discussion started: 21 January 2026

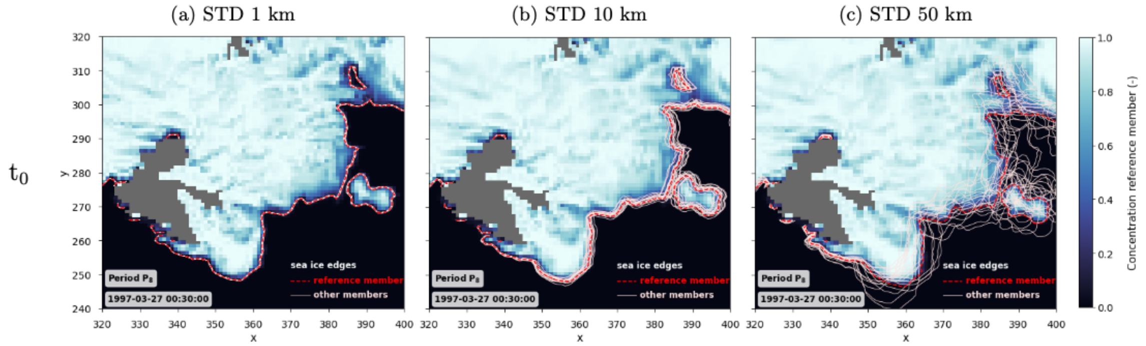

Figure 6. Initial spread of the local sea ice edge position in the Svalbard region during period P_8 (1997-03-27) for an initial perturbation scaled to a standard deviation (STD) of (a) 1 km, (b) 10 km, and (c) 50 km. The ice edge of the reference ensemble member (used here to illustrate the method) is indicated by a thick dashed red line, while the remaining 19 members are shown as thin pink lines. The corresponding hourly sea ice concentration field of the reference member is displayed in the background (shading).

nearly constant for the smallest initial perturbations), indicating that the ensemble members tend to converge towards a more similar sea ice edge position within the 10-day hindcast period (illustrated in Fig. 5b). Contrary to what might be expected from a chaotic behavior, no exponential growth of the error is observed for this metric. Instead, the initially-introduced positional errors of the ice edge are damped with time. The largest initial errors are typically reduced by about half within ten days of forecast, while the smallest perturbations—on the order of one-tenth of a model grid cell—remain nearly constant throughout the forecast period. However, the impact of initial errors persists through the 10-day forecasts, with the large initial errors leading to larger SPS errors after 10 days than the small initial errors. In that sense, some predictability in the position of the sea ice edge persists until the end of the 10 days. This behavior of the ensemble members to converge toward a similar sea ice edge position demonstrates the strong constraint exerted by the boundary conditions of the sea ice system on the ice edge position. In our configuration, only the sea ice is perturbed at initialization. The atmospheric forcing remains unperturbed: the same exact atmosphere is seen by all the ensemble members. The ocean component is also initially unperturbed but is coupled to the perturbed sea ice. However, at its resolution (1/4°, ~10 km in the Arctic), it does not seem to respond sufficiently to the local initial displacements of the ice-edge position to induce a growing spread of the ocean-ice solutions in the different ensemble members. However, it is possible that a higher-resolution ocean model—with more active mesoscale turbulence—could lead to a different behavior. Overall, these results indicate that the short-term evolution of the SPS in our simulations reflects primarily the deterministic adjustment of the ice edge position to the imposed oceanic and atmospheric boundary conditions (in common to all the ensemble members). In other words, we find that at the resolution of our system, forecast performance on the sea ice edge position depends more strongly on the quality of the external oceanic and atmospheric conditions than on an accurate initial position of the sea ice edge. This is also why the SPS error was found to grow with time-lag in fully coupled

https://doi.org/10.5194/egusphere-2025-6379
Preprint. Discussion started: 21 January 2026

(a) BBM

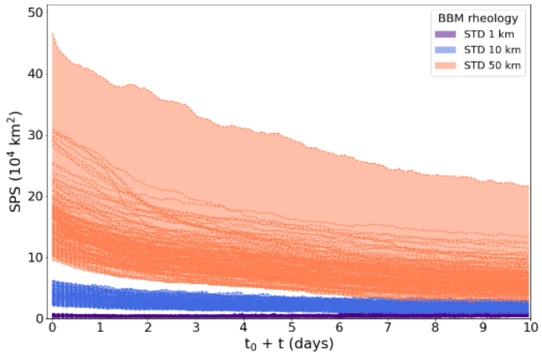

(b) aEVP

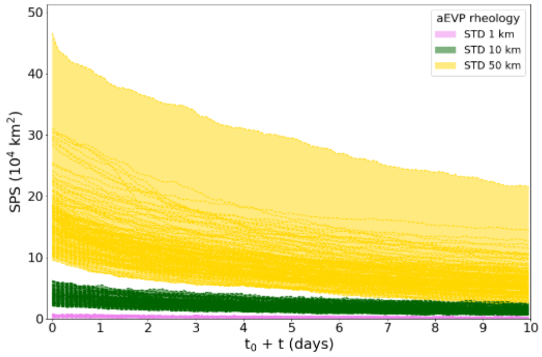

Figure 7. Temporal evolution of the SPS score computed over the whole Arctic, for BBM and aEVP hindcasts (a,b resp.). The plotted curves correspond to the SPS scores computed for each of the eight forecast periods, and for each ensemble member taken alternatively as the pseudo-truth, resulting in total in 8 Periods × 20 scores = 160 curves. The colors correspond to the three different amplitudes of initial perturbation.

atmosphere-sea-ice-ocean systems initialized with perturbed atmosphere and Sea Surface Temperature (e.g. Zampieri et al., 2018).

Finally, no significant differences are found in the predictability behavior of the SPS between the two rheologies explored in this study (Fig. 7). It suggests that, for short-term forecasts, the evolution of the sea ice edge position is more constrained by thermodynamic interactions with the underlying ocean and the above atmosphere than by internal dynamical processes.

https://doi.org/10.5194/egusphere-2025-6379
Preprint. Discussion started: 21 January 2026

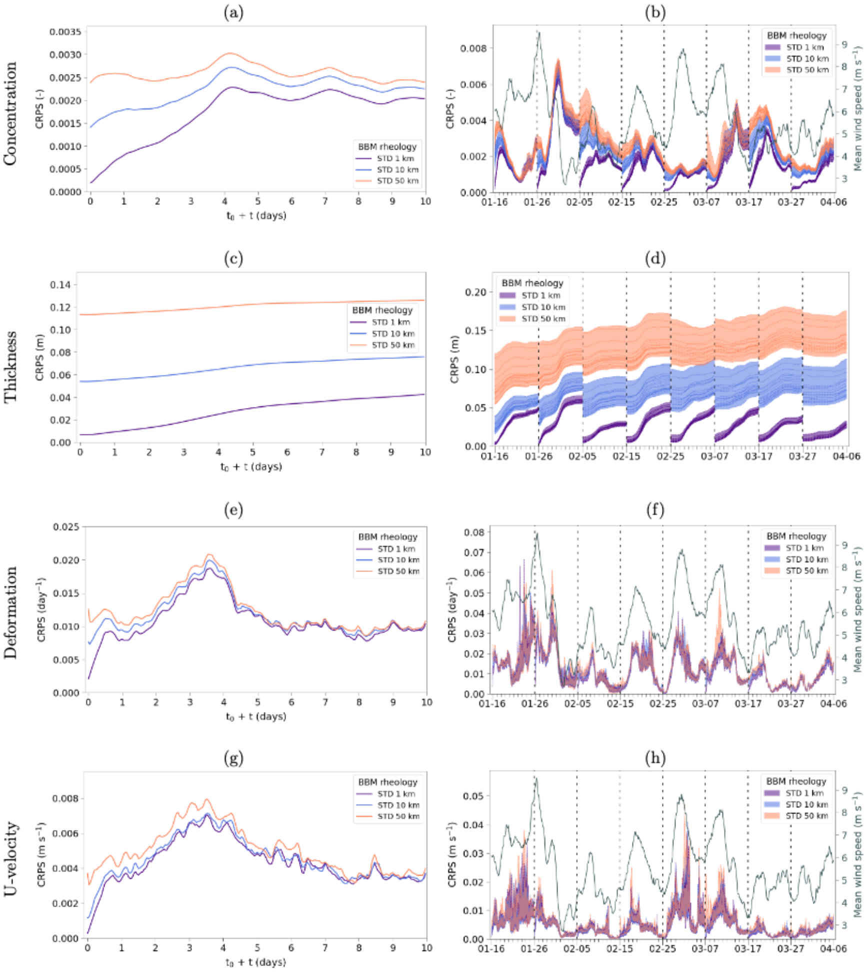

Figure 8. Temporal evolution of the CRPS metric in the BBM hincasts for the three types of initial perturbations, shown in average for the eight periods P_1,...P_8 (left column) and separately for each period (right column). The CRPS metric is computed for (a,b) sea ice concentration, (c,d) thickness, (e,f) deformation and (g,h) velocity along the x-axis. The colors correspond to the three amplitudes of initial perturbation. The solid line on (b, f, h) stands for the mean wind speed averaged over the same domain as the CRPS metrics (cf Fig. 1). The colored envelopes (right column) correspond to the min-to-max of the CRPS scores computed for each member taken alternatively as the pseudo-truth. The thin curves on panels (b) and (d) show the scores corresponding to each member taken alternatively as the pseudo-truth.

https://doi.org/10.5194/egusphere-2025-6379
Preprint. Discussion started: 21 January 2026

4.2 Predictability in the pack ice region

In this section, we extend the analysis to the predictability of some of the main dynamical and thermodynamical properties of the pack ice: sea ice concentration, thickness, drift, and deformation. Leads, pressure ridges, and high-deformation linear features are manifestations of the heterogeneity of winter fields that remain a challenge to accurately forecast (e.g. Mohammadi-Aragh et al., 2018; Korosov et al., 2023). We focus on the pack ice region as delimited in Fig. 2, excluding on purpose the coastal areas and the Marginal Ice Zone (MIZ), where landfast ice and small ice floes, respectively, might behave differently than the central pack ice with respect to predictability and would require adequate metrics. We evaluate here the forecast accuracy using the Continuous Ranked Probability Score (CRPS; e.g., Hersbach 2000), a widely-used metric in atmospheric and oceanic ensemble forecasting (e.g., Hersbach, 2000; Lang et al., 2024; Candille et al., 2015; Leroux et al., 2022). The CRPS provides a spatially-integrated measure of the grid-point mismatch between a probabilistic forecast and a reference value. It is defined as the expected value of Δ, calculated at each grid point as:

$$\Delta = \int_{-\infty}^{+\infty} |F(m) - F_{ref}(m)|\, dm \tag{2}$$

and in practice the expectation of Δ is approximated here by its spatial average over the region of interest (cf Fig.2). F is, at each point in the model grid, the cumulative distribution function of the predicted physical quantity m, and F_{ref} the reference function to compare with. In our perfect model ensemble approach, the reference value—or pseudo-truth—is alternately taken as each individual ensemble member, while the remaining 19 members are used to estimate the forecast distribution. F is defined as a stepwise function that increases by 1/19 at each of the 19 forecast values. F_{ref} is a Heaviside function that varies from 0 to 1 at the value of the reference member. Thus, Δ can be seen as the area between the two cumulative distribution functions, and the CRPS can be interpreted as a generalized absolute error for the ensemble forecasts, accounting for both the bias and the spread of the ensemble and sharing the same unit as the forecasted physical quantity. Note, however, that in the perfect-model context where the pseudo-truth is taken from the ensemble itself, the CRPS primarily reflects the ensemble spread, or in other words the forecast uncertainty.

In the following, we investigate the evolution of the CRPS for sea ice concentration, thickness, drift, and deformation on average and individually for the eight 10-day forecast periods P_1,...,P_8. The purpose is to quantify the evolution of the ensemble spread, i.e. the forecast uncertainty, in positioning accurately the heterogeneous features of the pack ice. We first investigate the results based on the Elasto-Brittle (BBM) experiments, and then we contrast these results with those based on the Elasto-Viscous (aEVP) experiments.

4.2.1 CRPS results from the brittle (BBM) model

We first focus on the concentration of sea ice, of which the evolution of CRPS is shown in Fig. 8a-b for the BBM-based hindcasts. On average (Fig. 8a), the positional errors introduced at initial time first trigger a growth phase of the CRPS over the first four days, after which a more stable phase is reached where the CRPS tends to level off. In contrast to what was found in the previous section for the sea-ice-edge score, this behaviour is indicative of a non-linear, chaotic-like response:

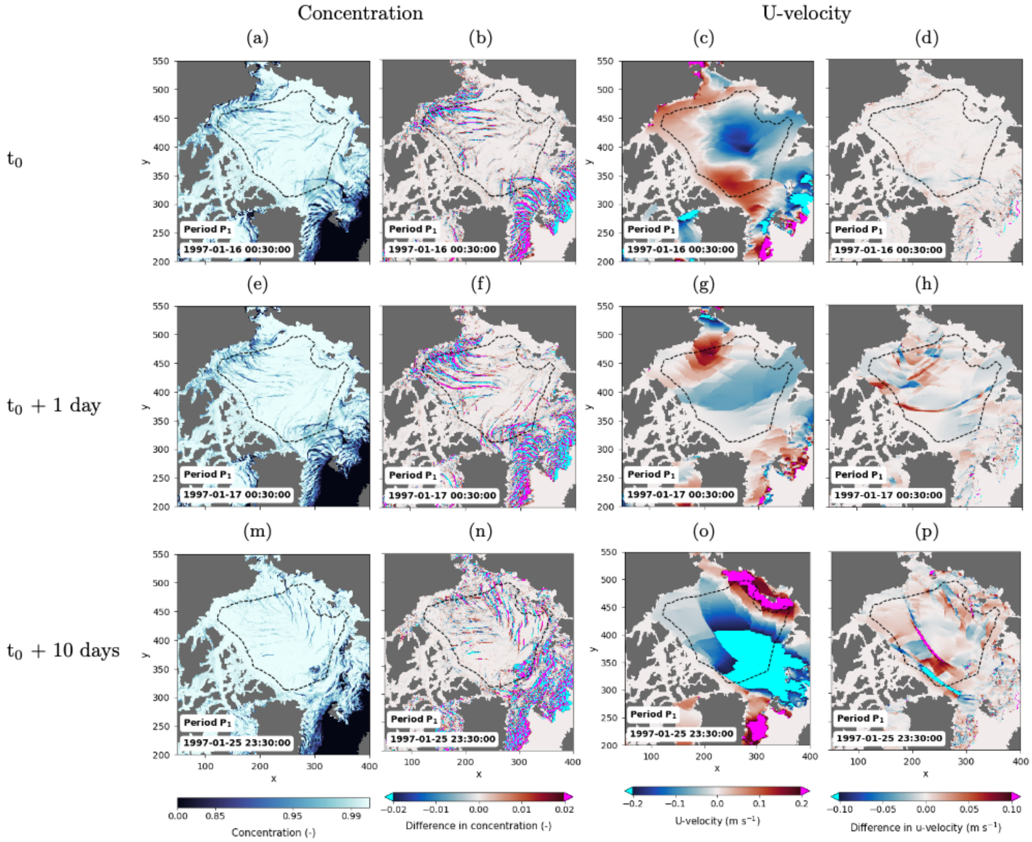

Figure 9. Sea-ice concentration and U-component of sea-ice velocity (a,e,m and c,g,o, resp.) from the BBM hindcasts initialized with the 10-km perturbation at three lead times during period P_1: (a–d) initial time, (e–h) after one day, and (m–p) after ten days. Panels (b,f,n) and (d,h,p) show, respectively, the differences in concentration and in the U-component of velocity between two perturbed ensemble members. The black dashed line defines the boundaries of the region over which the CRPS metric is computed.

even very small initial perturbations produce a rapid error growth that eventually reaches a saturation level. This saturation corresponds to a state in which ensemble members have become as dissimilar as possible according to the CRPS metric, despite being forced by identical atmospheric conditions. Put differently, two ensemble members initialized with the same individual leads—perturbed only slightly in their initial position—begin to diverge by first displacing the features present at t_0, and subsequently by generating new features that no longer form at exactly the same locations, even though they remain within the same broader region shaped by the surface wind forcing (Fig. 9).

https://doi.org/10.5194/egusphere-2025-6379
Preprint. Discussion started: 21 January 2026

Comparing the CRPS evolution of the three different amplitudes of initial perturbations (red, blue, and purple envelopes corresponding to the evolution of the large, medium, and small-amplitude perturbations, respectively, in Fig. 8a-b) helps to identify the lead time beyond which predictability is fully lost—that is, the point at which the three envelopes become indistinguishable and the initial errors no longer influence the forecast. For concentration, we find that on average, the three curves are not yet totally indistinguishable after 10 days, suggesting that some predictability remains at that time lag (on average). But this mainly reflects the fact that individual forecast periods show contrasting behaviors in this regard (Fig. 8b): for instance, the CRPS in P1 exhibits rapid error growth followed by convergence of the three envelopes after only about 5 days, while for periods P7 and P8, it takes longer for the envelopes to become indistinguishable, meaning that the impact of the initial error persists throughout the 10-day forecast in these cases. Individual periods reveal different levels of sensitivity to initial errors depending on the pre-existing states of the sea ice and the evolution of the atmospheric forcing: for a fixed amplitude of positional perturbation, more heterogeneous initial fields result in a larger initial CRPS. Or in other words, positional perturbations applied to an initially-uniform field will have little to no effect, whereas the same perturbations applied to a highly-heterogeneous field result in a larger CRPS, as each displaced feature contributes to the overall mismatch quantified by the CRPS. In addition, periods with high wind forcing or periods with calm conditions might influence differently the behavior and growth rate of the CRPS responding to the same initial error.

However, the key point here is that we find, for all the periods and in average, that the small-amplitude initial perturbations (purple envelopes) always induce a growth of the CRPS in the first few days, until it converges with the curves from the larger-amplitude perturbations in about 5 to 10 days, as expected from a non-linear, chaotic response.

The same kind of conclusions can be drawn from the evolution of CRPS of sea ice deformation and drift (Fig. 8e-f-g-h), where the growth phase lasts for about 4 days on average, after which the 3 curves for the 3 amplitudes of initial perturbation become indistinguishable. Note that the individual periods also show some diversity, even though less visible than for concentration: the three types of envelope have in some cases fully converged in a day or so (for example, P1 and P2) while it takes about 5 days in P5 or P6. In any case, it is striking from Fig. 8 that for deformation and drift, i.e. the physical fields resulting from the dynamical and rheological processes in sea ice, the sensitivity to initial error is strong in this model configuration based on the BBM rheological formulation, and predictability decreases drastically in only a few days, to be fully lost in about 5 days. This is consistent with previously-published studies that estimate the predictability horizon of LKFs to be 4-8 days by Mohammadi-Aragh et al. (2018); Korosov et al. (2023). But importantly, we show here that this predictability limit is reached in a model considered as perfect and forced by a perfect atmospheric forcing. Put differently, we demonstrate the non-linear, chaotic behavior of the sea ice system itself (as modeled in this configuration), without the need to invoke its interaction with the chaotic atmosphere.

The evolution of the CRPS for the thickness of sea ice (Fig. 8c-d) also confirms the growth phase of the initial small and medium perturbations, with the CRPS curves showing signs of slow convergence, on average. However, it takes much longer than for the other sea ice quantities: after 10 days, the CRPS level of the three types of initial perturbations has not converged, and in fact the three types of envelopes are not yet overlapping (Fig. 8d), meaning that some predictability remains at that time lag and that initial errors matter for the entire duration of the experiments. Note in Fig. 8d that the initial CRPS level of each

https://doi.org/10.5194/egusphere-2025-6379
Preprint. Discussion started: 21 January 2026

period gradually increases from P1 to P5. We explain this increase by the short spinup time of only 15 days before initializing the reference simulations from which the initial states P1-P8 are taken (see Sect. 2). It is likely too short for a realistic amount of heterogenities in the thickness field to be established in the model state spinning up from the smooth GLORYS reanalysis. From P1 to P5, the heterogenities in the initial thickness fields continue to grow in number (shown in the Appendix A, Fig. A1) and it explains why the initial CRPS level gradually increases from P1 to P5. It should be noted that for other quantities such as concentration, deformation, and drift, we do not see any impact of the short spinup either in the initial CRPS or in the initial fields of the P1–P8 periods, which do not exhibit any systematic trend in their degree of heterogeneity (shown in Appendix A, Figs. A1,A2). This supports a posteriori the view that a 15-day spinup is adequate to initialize the system for the predictability analysis conducted here.

4.2.2 CRPS results in the elasto-visco-plastic (aEVP) model

We now contrast the above BBM hindcast results with the corresponding CRPS results from the aEVP hindcasts, shown in Fig. 10. It should be reminded here that these aEVP ensemble hindcasts are initialized by exactly the same perturbed sea ice states as those for the BBM hindcasts. Those initial states are produced from the eight dates extracted from the reference BBM-based simulation and subsequently perturbed (see Sect. 2 for details). This choice ensures that the initial states include a realistic level of heterogenities and LKFs as would be the case in an operational system where some high-resolution observations were assimilated (as explored, for example, by Korosov et al. (2023) or Moro et al. (2024)). It means that by construction, the initial CRPS level is strictly equal in the aEVP and BBM hindcasts, which is verified in the panels for concentration and thickness comparing Fig. 10 to Fig. 8. Note, however, that in the latter figures, the value of the CRPS at t_0 for deformation and U-velocity is about five times smaller from aEVP than from BBM (note also that the y-axes have been re-scaled). This is because, as explained in the methodology section, the score plotted at t_0 in these figures is based on the first model output of the simulations, corresponding to the averaged model state over the first hour. Our results thus mean that in less than an hour, the model state in deformation and U-velocity in the aEVP hindcasts has already changed sufficiently, and ensemble members converged enough that the resulting CRPS has already decreased by a factor five compared to the first hour in the BBM hindcasts. More generally, for all four quantities considered (concentration, thickness, deformation and U-velocity) we find that the level of ensemble spread or forecast uncertainty, as measured by the CRPS metric, is smaller in the aEVP ensembles than in the BBM ensembles after initial time. Contrasting with the behavior observed for the BBM hindcasts in Fig. 8, Fig. 10 for the aEVP hindcasts reveals a clear decreasing trend of CRPS from the initial time to the end of the 10 days, for all four variables. This systematic decrease indicates a convergence of the model state in the ensemble members, as opposed to the non-linear behavior of the BBM hindcasts and their initial growing phase of the CRPS. We thus document here a contrasted sensitivity to initial positional errors depending on the rheology: unlike the BBM model, the model based on aEVP is not sensitive to initial errors related to misplacement of surface heterogeneities, and in fact it tends to reduce the level of heterogeneities introduced at initial time: a smoother aspect of the concentration and sea ice drift fields is already visible after just 1 day in Fig. 11), and most leads and heterogeneous features have disappeared by day 10 (comparing Figs. 9 and 11) even though both models are started from exactly the same initial conditions and forced with the same surface wind. The fields becoming less heterogeneous, fewer errors can accumulate in the CRPS metric, which becomes smaller with lead time.

The aEVP model is shown to be very little sensitive to the accuracy of the initial position of LKF features and much more predictable than the BBM model. But this comes at the price of smoother and less heterogeneous sea ice fields that do not sufficiently reflect its observed properties in the winter season (Ólason et al., 2022; Korosov et al., 2023). The BBM model by contrast is shown to be very sensitive to initial positional errors, and predictability is rapidely lost (in 1 to 5 days for drift and deformation, 5 to 10 days for concentration), meaning that the accurate position of the individual features (LKFs, leads, etc.) is not known after this lead time. This non-linear behavior is shown to arise from the nature of the rheology formulation, isolated by the experimental design from any other known sources of forecast uncertainty such as the atmospheric forcing or other uncertain parameters in the ice model. In practice, the effect of the latter will of course come and add up in the context of an operational system.

4.2.3 Probability maps of high-deformation events

As an illustration of the difference in the behavior of the two rheologies revealed by the CRPS metrics and of what this implies in practice, we show in Fig. 12 some example probability maps that indicate the likelihood of experiencing at least one high-deformation event within 24 hours in each model cell. High-deformation events are defined as those when the hourly deformation in a model cell exceeds a threshold set at the 95th percentile of the hourly deformation distribution during the winter season (January–March 1997) in the pack-ice region outlined in Fig. 1. This threshold approximately corresponds, for each rheology, to the deformation value above which the ice material enters the plastic regime in the aEVP case and the visco-elastic regime in the BBM case. In practice, it also marks the emergence of LKFs that can affect users operating in the field—for example, scientists that deploy, maintain or retrieve instruments on the ice, as during the MOSAiC campaign (Rabe et al., 2024). In that study, the authors reported significant deformation at one of their sites drifting on the pack ice near the North Pole in January–February 2020. In particular, they documented a large crack and subsequent pressure ridge developing across the site that impacted their instruments (see their figure 6).

Figure 12 shows that according to the BBM model, the chance of experiencing a high-deformation event at a given location during a given 24-hour period is high (probability greater than 90%, highlighted in yellow) in most parts of the central Arctic region under moderate-strong wind conditions. In contrast, according to the aEVP model, a significant fraction of the central Arctic exhibits a low risk of high-deformation events (probability lower than 20%, highlighted in purple), and the risk is concentrated in narrower areas (i.e. less uncertainty in the hindcasts of smoother deformation fields). This example highlights that, in some cases, lower predictability can nevertheless yield more informative assessments of the local risk of deformation events.

4.3 Predictability of Lagrangian trajectories

In this section, we complement the previous CRPS analysis, which evaluated the model skills in an Eulerian framework, by now considering predictability from a Lagrangian perspective. We showed in the previous section that, at the grid-cell level,

https://doi.org/10.5194/egusphere-2025-6379
Preprint. Discussion started: 21 January 2026

Figure 10. Same as Fig. 8 but for the CRPS metric from the aEVP hindcasts initialized with the 10-km perturbation.

the drift of sea ice becomes fully decorrelated between the ensemble members within a few days (1–5 days) in the BBM model, while in the aEVP configuration the members of the ensemble tend to converge towards a more similar and spatially

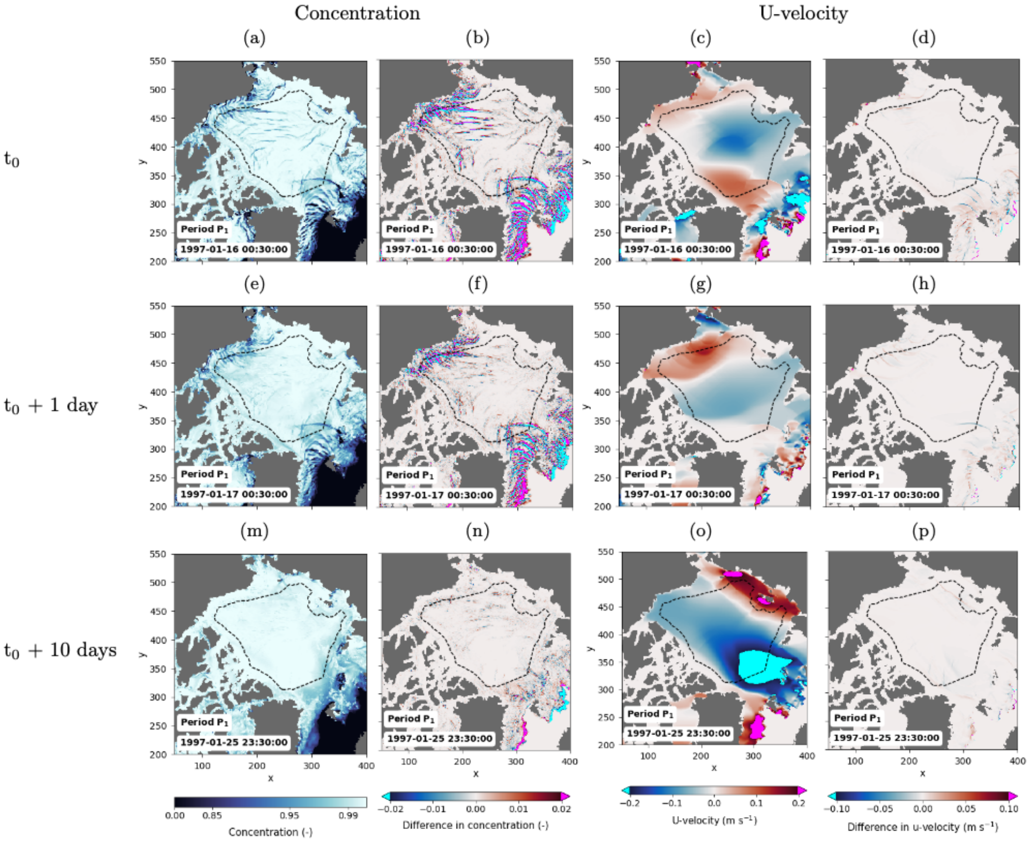

Figure 11. Same as Fig. 9 but from the aEVP hindcasts initialized with the 10-km perturbation.

smooth solution. Here, we document how these contrasting behaviors translate into the divergence of Lagrangian trajectories computed from the simulated sea-ice drift fields of the two configurations. Such Lagrangian metrics might be more meaningful in an operational context of search-and-rescue, for example. They also allow us to relate our approach more directly to the studies of Rabatel et al. (2018); Cheng et al. (2020).

455 We make use of the virtual buoys generated from all the ensemble hindcasts (i.e. the eight time periods and three perturbation amplitudes) with the two model configurations, as described in Sect. 3. An example of these virtual buoy trajectories is given in Fig. 13 and some statistics on the 101 ensembles of trajectories are provided in Fig. 14. More specifically, the figure displays the temporal evolution of the ensemble spread, measured by the area of the ellipse defined by the 95% confidence contour of the distribution (assumed to be bivariate normal). Note that the range of the y-axis is ten times larger in Fig. 14a than in Fig. 14b.

https://doi.org/10.5194/egusphere-2025-6379
Preprint. Discussion started: 21 January 2026

(a) BBM

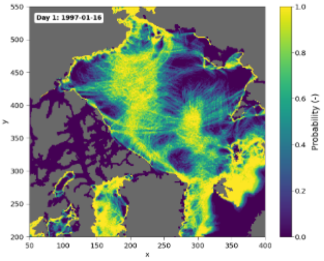

(b) aEVP

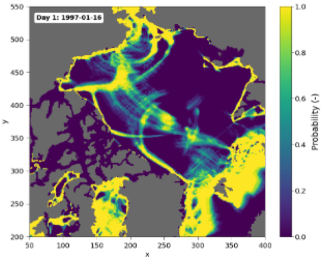

(c) BBM - aEVP

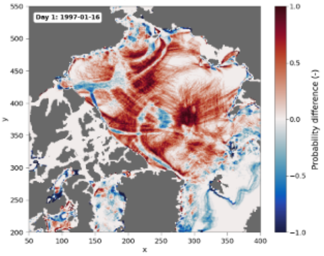

Figure 12. Maps illustrating the likelihood of experiencing at least one high-deformation event within 24 hours (here plotted for the first day of period P_1 as an illustration) in each model cell in the BBM and aEVP ensemble experiments (a,b resp.) intialized with STD = 50 km positional perturbations. The high-deformation events are defined as those when the hourly deformation in a model grid cell exceeds a threshold set at the 95th percentile of the hourly deformation distribution over the winter season in the pack-ice region (see text for details). Panel (c) shows the difference in probability between panels (a) and (b).

The spread between the virtual buoys grows with lead time for both BBM and aEVP models, as expected from passive tracers advected by velocity fields that themselves differ. Lagrangian trajectories accumulate differences at every time step because they are advected by distinct velocity fields in each ensemble member. Even in the case where the velocity fields of different ensemble members become more similar with lead time and the level of heterogeneity decreases (aEVP case), the Lagrangian trajectories still diverge because they integrate past differences along their paths. However, the statistics in Fig. 14 confirm

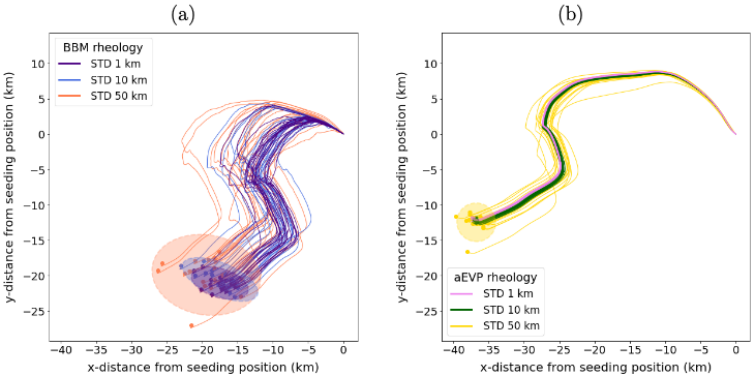

Figure 13. Example of virtual buoy trajectories simulated from the BBM and aEVP ensemble hindcasts (a,b, respectively) from an seeding on 7th March 1997 at midnight at -154.552° E and 74.886° N (red cross in Fig. 2). The coloured circles highlight the final positions after 10 days and the shaded ellipses represent the 95% confidence regions of the final positions, assuming a bivariate normal distribution. The colors correspond to the rheology and amplitude of the initial perturbation of the experiments.

what is already apparent from the example cases (Figs. 4 and 13): the spread of the virtual buoys grows significantly larger in the BBM configuration than in aEVP. After 10 days, the ellipse area is on average around 90 km^2 in the ensembles initialized with the larger perturbations (STD 50 km) and about 60 km^2 in the ensemble initialized with the smaller perturbations (STD 1 and 10 km). By contrast, the virtual buoys from the aEVP hindcasts have on average spread roughly an order of magnitude less: about 10 km^2 with the largest initial perturbation, while below 1 km^2 with the smaller initial perturbations. For reference, the dispersion found after 10 days in previous studies focused on the uncertainty caused by the surface wind or by some model parameters is approximately 800 km^2 and 200 km^2, respectively, in Cheng et al. (2020) (defined by the 99% confidence ellipse in their case) and 190 km^2 in Rabatel et al. (2018) from the wind uncertainty (scaled to a variance three times as small as in Cheng et al. (2020)). Our results thus confirm previous work that initial uncertainty has quantitatively less impact on the spread of Lagrangian trajectories than uncertainty in the wind forcing (at least when its variance is scaled as in Rabatel et al. (2018) and Cheng et al. (2020)). However, we also find that in the BBM configuration the effect of initial positional uncertainty on buoy dispersion is roughly an order of magnitude larger than in the aEVP configuration, making it comparable in magnitude to wind- and model-induced uncertainty. This implies that initial-condition uncertainty—when interacting with a highly sensitive rheology such as BBM—constitutes a non-negligible source of trajectory spread. In operational contexts such as search-and-rescue, where all sources of uncertainty accumulate along Lagrangian paths, this contribution may thus have important practical implications.

(a) BBM

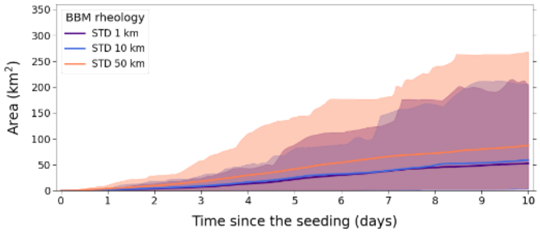

(b) aEVP

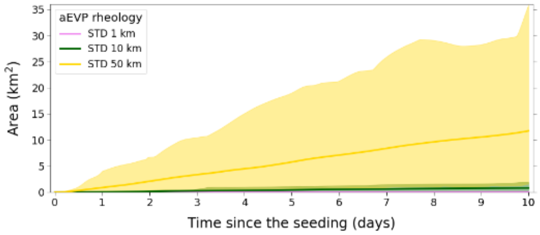

Figure 14. Temporal evolution of the spread of the virtual buoys from the BBM and aEVP ensemble hindcasts (a,b, resp.), as measured by the area of the ellipse defined by the 95% confidence contour of the distribution (assumed to be bivariate normal). The colors correspond to the rheology and amplitude of the initial perturbation of the experiment. The thick lines show the ensemble mean of all the buoys over all the eight 10-day periods, while the shaded envelopes indicate the 5%-to-95% percentile ensemble distribution. Panel (a) uses a y-axis range 10 times larger (area in km^2) than panel (b).

5 Summary and concluding remarks

Our study proposes an ensemble framework based on the SI3+NEMO sea ice ocean model with a horizontal resolution of 1/4° (∼10 km in the central Arctic) to investigate the predictability of the sea ice system on daily-to-weekly timescales, focusing on the sensitivity to initial uncertainty in the position of the sea ice features. We compare this sensitivity for two model configurations based on different formulations of sea ice rheology: the elastic–viscous–plastic (aEVP) formulation (Kimmritz et al., 2016) and the more recently developed brittle Bingham–Maxwell (BBM) formulation (Ólason et al., 2022). We examine the implications of these contrasting sensitivities for short-term winter sea-ice forecasting. Our experimental design isolates the response of the coupled ice–ocean system to initial positional uncertainty alone, deliberately excluding the additional uncertainty introduced through coupling with the atmosphere.

Our approach is based on 10-day ensemble hindcasts of N=20 members over eight non-overlapping time periods between the 16th of January and the 5th of April, 1997. Those ensemble hindcasts are initialized with perturbed initial states where Gaussian perturbation displacements $\Delta\mathrm{x}(x,y)$, $\Delta\mathrm{y}(x,y)$ in x and y directions are generated and applied consistently to all the sea ice variables, resulting in non-Gaussian perturbations of those variables to mimic mispositioned and distorted sea ice features (leads, LKFs, etc) that can arise at initialization in an operational system. The perturbations are scaled to different amplitudes of displacement (STD of 1, 10, and 50 km). In our approach, only the initial sea ice state is perturbed (the ocean is not), and exactly the same perturbed states are used to initialize the ensemble hindcasts with the BBM and aEVP rheology. A brief evaluation of the modeled sea ice drift against available Lagrangian sea ice IABP drifters confirmed that both configurations-BBM and aEVP-adequately reproduce the observed drift and provide an appropriate framework for comparing their sensitivity to initial conditions.

For the purpose of this study, we focus solely on initial errors as a source of uncertainty, excluding other significant and already documented sources of uncertainty such as surface wind forcing. Here, we consider the model and surface forcing as perfect and unperturbed for all members of the ensemble. We then assess potential predictability by measuring the response of the system, for a given evaluation metric, to small initial perturbations (misplacements of the order of 1/10th of a grid cell) as compared to larger errors (misplacements of tens of grid cells). We consider that the system has fully lost its potential predictability when the initial perturbations no longer have an impact on the level of divergence of the ensemble solutions. In practice, this happens at the lead time when the ensemble members initialized with slightly perturbed conditions have become as spread as when initialized with large perturbations.

This approach is applied to several commonly-used metrics, each highlighting a different aspect of the sea-ice hindcasts: (i) the Spatial Probability Score (SPS), a probabilistic integrated measure of local positional errors of the ice edge; (ii) the Continuous Ranked Probability Score (CRPS) for concentration, thickness, drift, and deformation, which provides a generalized absolute-error metric for ensemble forecasts, integrated over the pack-ice region; and (iii) Lagrangian metrics quantifying the spread of virtual sea-ice drifter trajectories generated from the ensemble simulations.

Our analysis first shows that short-term forecasts of the sea-ice edge do not show a non-linear, chaotic-like response to small positional uncertainties. Instead, initial errors tend to decay, reflecting a strong constraint from the imposed atmospheric forcing and the ocean's state. After 10 days, the forecasts still retain a memory of the initial error amplitude, while the ensemble members tend to converge toward a more similar ice-edge position. We found that this behavior is largely independent of rheology, indicating that ice-edge predictability in our system is primarily controlled by thermodynamic forcing rather than internal ice dynamics. In that regard, improving operational forecasts of the sea-ice edge is unlikely to be achieved through a changed rheology or through more accurate assimilation of its observed initial position alone, but rather through better initialization of the underlying ocean and more realistic atmospheric forcing—at least at the present model resolution. However, at higher resolution, a more turbulent ocean circulation that includes better-resolved mesoscale features may introduce additional nonlinearity in the coupled ice–ocean response, potentially increasing the sensitivity to initial position errors.

However, the CRPS metric for concentration, deformation, and drift display a strong non-linear, chaotic-like sensitivity to initial positional errors when using the BBM-based model. For these quantities, predictability rapidly degrades, and the CRPS evolution forgets about the initial perturbations after only a few days: five to ten days for concentration, one to five days for deformation and drift, and longer than 10 days for thickness. This intrinsic limit arises even under perfect atmospheric forcing, demonstrating that the sea-ice dynamics themselves can set a short predictability horizon for LKFs and dynamical features, before its interaction with the chaotic atmosphere.

In contrast, the system based on the aEVP rheology exhibits little sensitivity to positional errors: heterogeneities are quickly smoothed out, the ensemble members converge, and the CRPS metric decreases with lead time. Although this implies higher potential predictability, it reflects a loss of dynamical variability and a weaker representation of the observed sea-ice heterogeneity.

Note that in operational systems aiming to take into account all major sources of uncertainty, the surface wind forcing uncertainty should be considered as well and would introduce its own constraints on the predictability limits of the system (known to be one to two weeks in the atmosphere; e.g., Lorenz 1969). Surface wind uncertainty could be approached as in previous studies using a perturbation method (Cheng et al., 2020), using ensemble atmospheric analyses or forecasts Mohammadi-Aragh et al. (2018), or even coupling the sea-ice model to an atmosphere or atmospheric boundary-layer model, which would relax the current assumption of prescribed unidirectional atmospheric forcing and allow atmosphere–ice feedbacks to shape the forecast uncertainty more realistically. Noteworthy, the modelling framework used here is fully adequate to include, in possible future work, several additional sources of uncertainty to initial conditions, including wind forcing or other model parameters, and to compare, in a single framework, their respective impacts.

In practical applications, these potential predictability limits we highlighted lead the two types of rheology to produce very different levels of uncertainty in both the local probability of high-deformation events and the dispersion of Lagrangian trajectories. The BBM configuration generates strong, weakly predictable heterogeneities in the deformation fields, which translate into a high probability of encountering at least one intense deformation event (LKF formation) within 24 hours over large areas of the central Arctic. By contrast, the aEVP configuration produces much smoother deformation fields, leading to narrow zones of elevated risk surrounded by broad regions where the likelihood of such events remains low. Similarly, virtual-buoy experiments show that initial uncertainties in the sea ice Eulerian fields amplify rapidly under BBM dynamics—resulting in one order-of-magnitude larger Lagrangian spread than in aEVP after 10 days—whereas the aEVP system largely damps these initial differences.

The differences in the predictability behavior we have documented in this study are not merely academic, they also directly matter for practical applications, such as field operations or search-and-rescue response, where understanding uncertainty is often as important as the forecast itself (e.g. Tietsche et al., 2020). A system that strongly amplifies small initial errors (as documented here for BBM) may offer lower deterministic predictability yet provides more realistic—and therefore more useful—information about the range of plausible trajectories or the local likelihood of severe deformation. Conversely, a system that smooths heterogeneity (as in aEVP) may appear more predictable and also easier to handle for technical operational purposes (e.g. Data Assimilation), but it risks underestimating extreme outcomes. Such contrasts reinforce the value of ensemble forecasting for sea ice: in a highly nonlinear and only weakly predictable medium, ensembles provide not only an estimate of the forecast state but also a quantification of the risk associated with user-relevant events.

Code and data availability. The entire dataset of ensemble hindcasts represents 13 TB and is available upon request (stephanie.leroux@datlas.fr). The Lagrangian trajectories produced from the ensemble hindcasts represent 133 MB and are published on Zenodo (Fiol et al., 2025). The present work is based on several open-source packages (see text): the Lu simulator (Brankart and Leroux, 2025) https://github.com/cmems-arcticbliss/lu-simulator, Sitrack (Brodeau, 2025) https://github.com/brodeau/sitrack, ENSDAM https://github.com/brankart/ensdam. All the scripts used for the present paper (analyses and plots) are also made available on Zenodo: Fiol (2025).

Author contributions. LF, SL wrote the paper with contributions from PR and JMB. SL, PR and JMB initiated the study, LF carried out all the analysis work, based on the ensemble simulations run by SL. Interpretation of the results are from LF, SL and PR. JMB and SL developed the Lu Simulator to introduce initial positional uncertainty.

Competing interests. The authors declare that they have no conflict of interest.

Acknowledgements. This work was supported by HPC and storage resources provided by GENCI at IDRIS thanks to the grants 2024-A0170112020 and 2025-A0190416878 on the supercomputer Jean Zay's CSL partition. It was part of the Arctic-BLISS project (2024-2026) funded by the Copernicus Marine Service Evolution program. The Copernicus Marine Service is implemented by Mercator Ocean in the framework of a delegation agreement with the European Union. Some of the modeling developments for this work were also supported by the SASIP project (grant n° G-24-6778) through the VESRI program funded by Schmidt Sciences–a philanthropic initiative that seeks to improve societal outcomes through the development of emerging science and technologies. The authors wish to thank Y. Ying, L. Bertino, E. Olason, A. Korosov from the Nansen Environmental and Remote Sensing Center in Bergen for some insightful discussions that contributed to the initiation of this work, and L. Brodeau from IGE in Grenoble for his help with the Sitrack package. An AI-based language model was used to support English-language editing and improve textual fluency in parts of the manuscript, while all scientific content, interpretations, and conclusions remain the sole responsibility of the authors.

Appendix A: Initial states of periods P1 to P8

This Appendix section provides two supplementary figures illustrating the initial states of the eight periods P_1,...,P_8 in terms of sea ice thickness (Fig. A1) and concentration (Fig. A2).

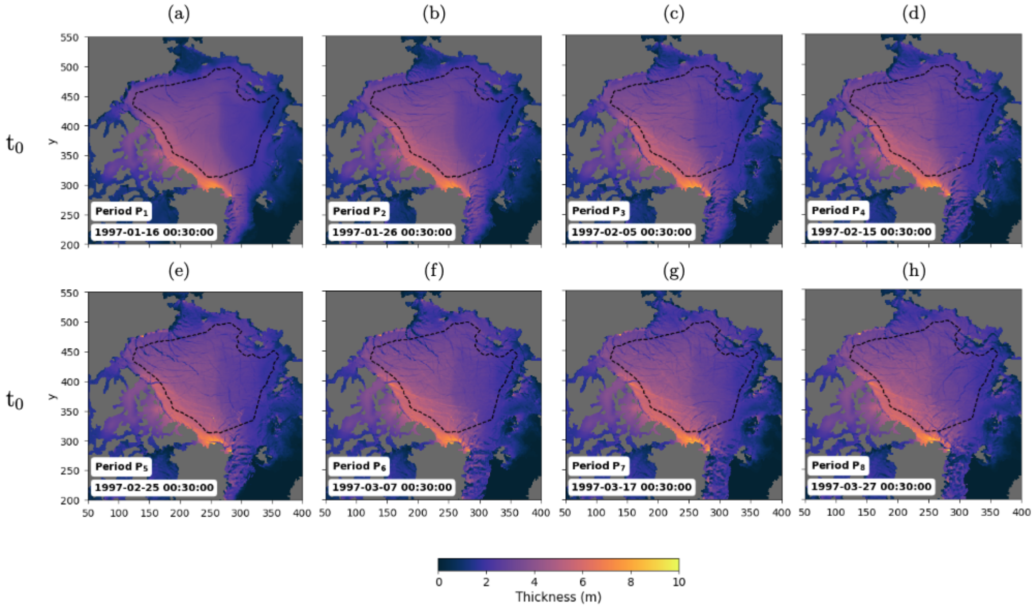

Figure A1. Sea ice thickness maps at initial time (t_0) of each period P_1,...,P_8 from the reference (unperturbed) experiment (see Sect. 2 for more details). The black dashed line defines the boundaries of the region over which the CRPS metric is computed in Sect. 4.2.

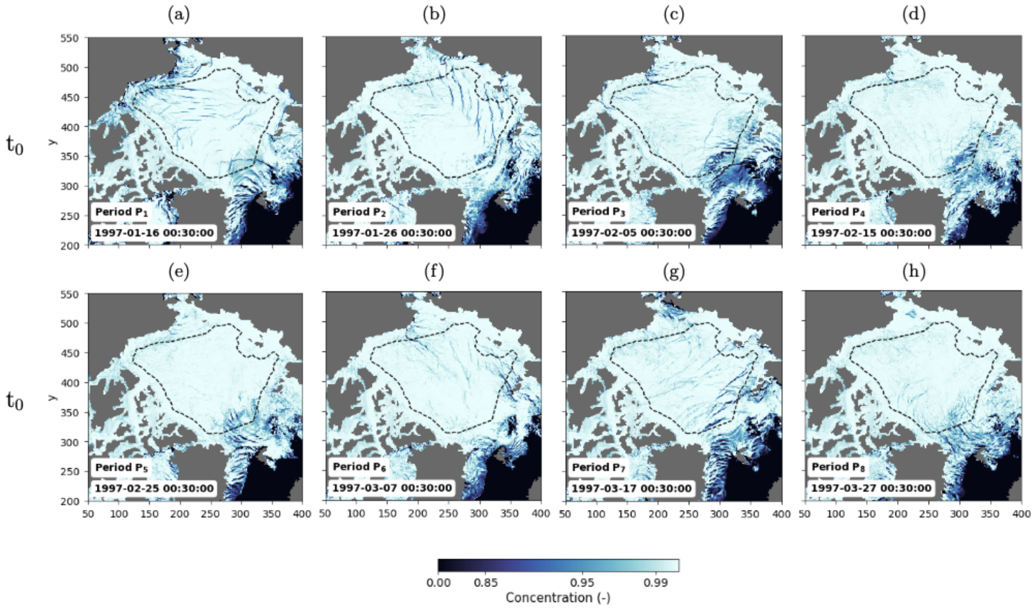

Figure A2. Sea ice concentration maps at initial time (t_0) of each period P_1,...,P_8 from the reference (unperturbed) experiment (see Sect. 2 for more details). The black dashed line defines the boundaries of the region over which the CRPS metric is computed in Sect. 4.2.

References

Bertino, L., Heimbach, P., Blockley, E., and Ólason, E.: Numerical models for monitoring and forecasting sea ice: a short description of present status, in: Ocean prediction: present status and state of the art (OPSR), edited by Álvarez Fanjul, E., Ciliberti, S. A., Pearlman, J., Wilmer-Becker, K., and Behera, S., vol. 5-opsr of *State Planet*, p. 14, Copernicus Publications, https://doi.org/10.5194/sp-5-opsr-14-2025, 2025.

Brankart, J.-M. and Leroux, S.: lu-simulator (v1.0), https://doi.org/10.5281/zenodo.17896830, 2025.

Brodeau, L.: sitrack: 1.1, https://doi.org/10.5281/zenodo.17942142, 2025.

Brodeau, L., Rampal, P., Ólason, E., and Dansereau, V.: Implementation of a brittle sea ice rheology in an Eulerian, finite-difference, C-grid modeling framework: impact on the simulated deformation of sea ice in the Arctic, Geoscientific Model Development, 17, 6051–6082, https://doi.org/10.5194/gmd-17-6051-2024, 2024.

Candille, G., Brankart, J.-M., and Brasseur, P.: Assessment of an ensemble system that assimilates Jason-1/Envisat altimeter data in a probabilistic model of the North Atlantic ocean circulation, Ocean Science, 11, 425–438, https://doi.org/10.5194/os-11-425-2015, 2015.

Cheng, S., Aydoğdu, A., Rampal, P., Carrassi, A., and Bertino, L.: Probabilistic forecasts of sea ice trajectories in the Arctic: impact of uncertainties in surface wind and ice cohesion, Oceans, 1, 326–342, https://doi.org/10.3390/oceans1040022, 2020.

Cruz-García, R., Goessling, H. F., Jung, T., Guemas, V., and Baehr, J.: Sources of Arctic sea ice area, extent, and volume predictability in a dynamical forecast system, The Cryosphere, 13, 491–509, https://doi.org/10.5194/tc-13-491-2019, 2019.

Dansereau, V., Weiss, J., Saramito, P., Lattes, P., and Coche, E.: Ice bridges and ridges in the Maxwell-EB sea ice rheology, The Cryosphere, 11, 2033–2058, https://doi.org/10.5194/tc-11-2033-2017, 2017.

Day, J. J., Tietsche, S., and Hawkins, E.: Pan-Arctic and regional sea ice predictability: Initialization month dependence, Journal of Climate, 27, 4371–4390, https://doi.org/10.1175/JCLI-D-13-00614.1, 2014.

Fiol, L.: Notebooks of the figures of Fiol et al. 2026 (v1.0), https://doi.org/10.5281/zenodo.17896832, 2025.

Fiol, L., Leroux, S., and Rampal, P.: Lagrangian trajectory dataset used in Fiol et al. 2026 (v1.0), https://doi.org/10.5281/zenodo.17897059, 2025.

Girard, L., Bouillon, S., Weiss, J., Amitrano, D., Fichefet, T., and Legat, V.: A new modeling framework for sea-ice mechanics based on elasto-brittle rheology, Annals of Glaciology, 52, 123–132, https://doi.org/10.3189/172756411795931499, 2011.

Goessling, H. F. and Jung, T.: A probabilistic verification score for contours: Methodology and application to Arctic ice-edge forecasts, Quarterly Journal of the Royal Meteorological Society, 144, 735–743, https://doi.org/10.1002/qj.3242, 2018.

Goessling, H. F., Tietsche, S., Day, J. J., Hawkins, E., and Jung, T.: Predictability of the Arctic sea ice edge, Geophysical Research Letters, 43, 1642–1650, https://doi.org/10.1002/2015GL067232, 2016.

Hersbach, H.: Decomposition of the Continuous Ranked Probability Score for Ensemble Prediction Systems, Weather and Forecasting, 15, 559–570, https://doi.org/10.1175/1520-0434(2000)015<0559:DOTCRP>2.0.CO;2, 2000.

Hersbach, H., Bell, B., Berrisford, P., Hirahara, S., Horányi, A., Muñoz-Sabater, J., Nicolas, J., Peubey, C., Radu, R., Schepers, D., Simmons, A., Soci, C., Abdalla, S., Abellan, X., Balsamo, G., Bechtold, P., Biavati, G., Bidlot, J., Bonavita, M., De Chiara, G., Dahlgren, P., Dee, D., Diamantakis, M., Dragani, R., Flemming, J., Forbes, R., Fuentes, M., Geer, A., Haimberger, L., Healy, S., Hogan, R. J., Hólm, E., Janisková, M., Keeley, S., Laloyaux, P., Lopez, P., Lupu, C., Radnoti, G., de Rosnay, P., Rozum, I., Vamborg, F., Villaume, S., and Thépaut, J.: The ERA5 global reanalysis, Quarterly Journal of the Royal Meteorological Society, 146, 1999–2049, https://doi.org/10.1002/qj.3803, 2020.

Hibler, W. D.: A dynamic thermodynamic sea ice model, Journal of Physical Oceanography, 9, 815–846, https://doi.org/10.1175/1520-0485(1979)009<0815:ADTSIM>2.0.CO;2, 1979.

Hunke, E. C. and Dukowicz, J. K.: An elastic–viscous–plastic model for sea ice dynamics, Journal of Physical Oceanography, 27, 1849–1867, https://doi.org/10.1175/1520-0485(1997)027<1849:AEVPMF>2.0.CO;2, 1997.

International Arctic Buoy Programme (IABP): In Situ Observations from the International Arctic Buoy Programme (IABP), Level 1, https://doi.org/10.18739/A2R785R0C, 2023.

Kimmritz, M., Danilov, S., and Losch, M.: The adaptive EVP method for solving the sea ice momentum equation, Ocean Modelling, 101, 59–67, https://doi.org/10.1016/j.ocemod.2016.03.004, 2016.

Korosov, A., Rampal, P., Ying, Y., Ólason, E., and Williams, T.: Towards improving short-term sea ice predictability using deformation observations, The Cryosphere, 17, 4223–4240, https://doi.org/10.5194/tc-17-4223-2023, 2023.

Kwok, R.: Deformation of the Arctic Ocean sea ice cover between November 1996 and April 1997: A quantitative study, Journal of Geophysical Research: Oceans, 106, 11 529–11 542, https://doi.org/10.1029/2000JC000061, 2001.

Kwok, R., Schweiger, A., Rothrock, D. A., Pang, S., and Kottmeier, C.: Sea ice motion from satellite passive microwave imagery assessed with ERS SAR and buoy motions, Journal of Geophysical Research: Oceans, 103, 8191–8214, https://doi.org/10.1029/97JC03334, 1998.

Lang, S. et al.: AIFS-CRPS: Ensemble forecasting using a model trained with a loss function based on the Continuous Ranked Probability Score, arXiv preprint arXiv:2412.15832, available at: https://arxiv.org/abs/2412.15832, 2024.

Lavergne, T. and Down, E.: A climate data record of year-round global sea-ice drift from the EUMETSAT Ocean and Sea Ice Satellite Application Facility (OSI SAF), Earth System Science Data, 15, 5807–5834, https://doi.org/10.5194/essd-15-5807-2023, 2023.

Lellouche, J.-M., Greiner, E., Bourdallé-Badie, R., Garric, G., Melet, A., Drévillon, M., Bricaud, C., Hamon, M., Le Galloudec, O., Regnier, C., Candela, T., Testut, C.-E., Gasparin, F., Ruggiero, G., Benkiran, M., Drillet, Y., and Le Traon, P.-Y.: The Copernicus Global 1/12° Oceanic and Sea Ice GLORYS12 Reanalysis, Frontiers in Earth Science, 9, 698 876, https://doi.org/10.3389/feart.2021.698876, 2021.

Leroux, S., Brankart, J.-M., Albert, A., Brodeau, L., Molines, J.-M., Jamet, Q., Le Sommer, J., Penduff, T., and Brasseur, P.: Ensemble quantification of short-term predictability of the ocean dynamics at a kilometric-scale resolution: a Western Mediterranean test case, Ocean Science, 18, 1619–1644, https://doi.org/10.5194/os-18-1619-2022, 2022.

Lorenz, E. N.: The predictability of a flow which possesses many scales of motion, Tellus, 21, 289–307, https://doi.org/10.1111/j.2153-3490.1969.tb00444.x, 1969.

Lorenz, E. N.: Climatic Predictability, in: The Physical Bases of Climate and Climate Modelling, no. 16 in GARP Publications Series, pp. 132–136, World Meteorological Organization, 1975.

Madec, G. and the NEMO-System-Team: NEMO Ocean Engine Reference Manual, NEMO consortium, doi: 10.5281/zenodo.1464816, 2024.

Mohammadi-Aragh, M., Goessling, H., Losch, M., Hutter, N., and Jung, T.: Predictability of Arctic sea ice on weather time scales, Scientific Reports, 8, 6514, https://doi.org/10.1038/s41598-018-24660-0, 2018.

Moro, M. D., Sperrevik, A. K., Lavergne, T., Bertino, L., Gusdal, Y., Iversen, S. C., and Rusin, J.: Assimilation of satellite swaths versus daily means of sea ice concentration in a regional coupled ocean–sea ice model, The Cryosphere, 18, 1597–1619, https://doi.org/10.5194/tc-18-1597-2024, 2024.

Ólason, E., Boutin, G., Korosov, A., Rampal, P., Williams, T., Kimmritz, M., et al.: A new brittle rheology and numerical framework for large-scale sea-ice models, Journal of Advances in Modeling Earth Systems, 14, e2021MS002 685, https://doi.org/10.1029/2021MS002685, 2022.

PAME: Arctic Shipping Status Report 1, Technical report, Protection of the Arctic Marine Environment (PAME), https://pame.is/images/03_Projects/ASSR/ASSR_1_-_2024_update.pdf, accessed September 2025, 2024.

Rabatel, M., Rampal, P., Carrassi, A., Bertino, L., and Jones, C. K. R. T.: Impact of rheology on probabilistic forecasts of sea ice trajectories: application for search and rescue operations in the Arctic, The Cryosphere, 12, 935–950, https://doi.org/10.5194/tc-12-935-2018, 2018.

Rabe, B. et al.: The MOSAiC Distributed Network: Observing the coupled Arctic system with multidisciplinary, coordinated platforms, Elementa: Science of the Anthropocene, 12, https://doi.org/10.1525/elementa.2023.00103, 2024.

Rampal, P.: Etude de la dérive et de la déformation de la banquise Arctique par l'analyse de trajectoires lagrangiennes, Ph.D. thesis, Université Joseph Fourier - Grenoble 1, français. tel-00352799, https://theses.hal.science/tel-00352799v1, 2008.

Rampal, P., Weiss, J., Marsan, D., Lindsay, R., and Stern, H.: Scaling properties of sea ice deformation from buoy dispersion analysis, Journal of Geophysical Research: Oceans, 113, C03 002, https://doi.org/10.1029/2007jc004143, 2008.

Rampal, P., Bouillon, S., Ólason, E., and Morlighem, M.: neXtSIM: a new Lagrangian sea ice model, The Cryosphere, 10, 1055–1073, https://doi.org/10.5194/tc-10-1055-2016, 2016.

Rampal, P., Dansereau, V., Olason, E., Bouillon, S., Williams, T., Korosov, A., and Samaké, A.: On the multi-fractal scaling properties of sea ice deformation, The Cryosphere, 13, 2457–2474, https://doi.org/10.5194/tc-13-2457-2019, 2019.

Reifenberg, S. F. and Goessling, H. F.: Predictability of Arctic sea ice drift in coupled climate models, The Cryosphere, 16, 2927–2946, https://doi.org/10.5194/tc-16-2927-2022, 2022.

Sakov, P., Counillon, F., Bertino, L., Lisæter, K. A., Oke, P. R., and Korablev, A.: TOPAZ4: an ocean-sea ice data assimilation system for the North Atlantic and Arctic, Ocean Science, 8, 633–656, https://doi.org/10.5194/os-8-633-2012, 2012.

Simonsen, M., Hackett, B., Bertino, L., Røed, L. P., Waagbø, G. A., Drivdal, M., and Sutherland, G.: Product User Manual For Arctic Ocean Physical and Bio Analysis and Forecasting Products ARCTIC_ANALYSIS_FORECAST_PHYS_002_001_A ARCTIC_ANALYSIS_FORECAST_BIO_002_004 ARCTIC_REANALYSIS_PHYS_002_003 ARCTIC_REANALYSIS_BIO_002_005, Tech. rep., CMEMS-ARC-PUM-002-ALL, Norwegian Meteorological Institute, 2018.

Tietsche, S., Day, J. J., Collins, M., and Hawkins, E.: Predictability of the Arctic sea ice edge, Geophysical Research Letters, 41, 2414–2420, https://doi.org/10.1002/2014GL059393, 2014.

Tietsche, S., Mueller, M., Bertino, L., Garric, G., Goessling, H., Pedersen, L. T., Wagner, P., and Lavergne, T.: Recommendations for more user-relevant sea-ice forecasts, Public technical report, deliverable d4.3, EU-KEPLER project, https://kepler-polar.eu/deliverables/index.html, accessed September 2025, 2020.

Vancoppenolle, M., Rousset, C., Blockley, E., and the NEMO Sea Ice Working Group: SI3 – Sea Ice modelling Integrated Initiative – The NEMO Sea Ice Engine, Zenodo, doi: 10.5281/zenodo.7534900, 2023.

Williams, T., Korosov, A., Rampal, P., and Ólason, E.: Presentation and evaluation of the Arctic sea ice forecasting system neXtSIM-F, The Cryosphere, 15, 3207–3227, https://doi.org/10.5194/tc-15-3207-2021, 2021.

Zampieri, L., Goessling, H. F., and Jung, T.: Predictability of Arctic sea ice edge on weather and climate time scales, Geophysical Research Letters, 45, 9900–9908, https://doi.org/10.1029/2018GL079394, 2018.